

Article

MIMO-SAR Interferometric Measurements for Wind Turbine Tower Deformation Monitoring

Andreas Baumann-Ouyang ^{1,2,*} , Jemil Avers Butt ^{1,3} , Matej Varga ¹  and Andreas Wieser ¹ ¹ Institute of Geodesy and Photogrammetry, ETH Zürich, 8093 Zürich, Switzerland² RUAG AG, 8602 Wangen, Switzerland³ Atlas Optimization GmbH, 8049 Zürich, Switzerland

* Correspondence: andreas.baumann@geod.baug.ethz.ch; Tel.: +41-44-633-30-53

Abstract: Deformations affect the structural integrity of wind turbine towers. The health of such structures is thus assessed by monitoring. The majority of sensors used for this purpose are costly and require in situ installations. We investigated whether Multiple-Input Multiple-Output Synthetic Aperture Radar (MIMO-SAR) sensors can be used to monitor wind turbine towers. We used an automotive-grade, low-cost, off-the-shelf MIMO-SAR sensor operating in the W-band with an acquisition frequency of 100 Hz to derive Line-Of-Sight (LOS) deformation measurements in ranges up to about 175 m. Time series of displacement measurements for areas at different heights of the tower were analyzed and compared to reference measurements acquired by processing video camera recordings and total station measurements. The results showed movements in the range of up to 1 m at the top of the tower. We were able to detect the deformations also with the W-band MIMO-SAR sensor; for areas with sufficient radar backscattering, the results suggest a sub-mm noise level of the radar measurements and agreement with the reference measurements at the mm- to sub-mm level. We further applied Fourier transformation to detect the dominant vibration frequencies and identified values ranging from 0.17 to 24 Hz. The outcomes confirmed the potential of MIMO-SAR sensors for highly precise, cost-efficient, and time-efficient structural monitoring of wind turbine towers. The sensors are likely also applicable for monitoring other high-rise structures such as skyscrapers or chimneys.

Keywords: wind turbine; monitoring; radar; MIMO-SAR; interferometry; total station; camera

Citation: Baumann-Ouyang, A.; Butt, J.A.; Varga, A.; Wieser, A. MIMO-SAR Interferometric Measurements for Wind Turbine Tower Deformation Monitoring. *Energies* **2023**, *16*, 1518. <https://doi.org/10.3390/en16031518>

Academic Editors: Francesc Pozo and Yolanda Vidal

Received: 9 January 2023

Revised: 29 January 2023

Accepted: 1 February 2023

Published: 3 February 2023



Copyright: © 2023 by the authors. Licensee MDPI, Basel, Switzerland. This article is an open access article distributed under the terms and conditions of the Creative Commons Attribution (CC BY) license (<https://creativecommons.org/licenses/by/4.0/>).

1. Introduction

Wind turbines played a significant role in increasing the production of electric energy from renewable sources by a factor of about 15 (to 35.8 EJ) between 2000 and 2021 [1]. The increased size of rotor diameters and hub heights of wind turbines [2] has helped raise the turbines' capacities. However, the increased dimensions of the turbines not only have increased the energy yield, but have also caused more significant loads on the structures [3]. This load impacts the structural integrity of the turbines and the towers [4]. Measuring the dynamic deformation of a tower can help to assess and predict the structure's health in the context of Structural Health Monitoring (SHM). In [5], it was reported that a wind turbine tower of 40 m had vibration modes ranging from 0.7 to 18 Hz for the first and eighth modes, respectively. Generally, wind turbines have a first natural frequency below 1 Hz [6,7]. Strain gauges and accelerometers are the most-common types of sensors utilized for the SHM of wind turbine towers [8–10]. They must be installed at certain heights to measure the vibration modes effectively, which is not always possible due to limited accessibility. Additionally, the sensors need to have low measurement noise and high temporal resolution for the identification of these frequencies [11] and are thus typically expensive [8,12].

Several proposals for using remote sensing techniques for monitoring structures have been made in the literature, including laser Doppler vibrometry [13], terrestrial laser

scanning [14,15], photogrammetry [16,17], and terrestrial real aperture radar interferometry [18,19]. Some of those solutions require the installation of (reflective) targets on the tower (e.g., [13,16,17]), the setup of multiple sensors around the tower (e.g., [14,16]), or using expensive equipment (e.g., [14,18,19]). MIMO-SAR, or Multiple-Input Multiple-Output Synthetic Aperture Radar, is a novel technology with attractive properties for remote SHM [20,21]. In recent years, the autonomous driving industry has been pushing its development, since it allows for compact design, low mechanical complexity (no moving parts), and low hardware cost. Moreover, it facilitates high angular and range resolution [22] and can acquire measurements of an entire scene instantaneously, even under adverse weather conditions [23]. MIMO-SAR sensors have already been applied successfully in SHM, e.g., to measure the high-frequency deformations of bridges [20,24–26], detecting the low-frequency deformations of buildings and slopes in open-pit mines [21,27], mapping large cracks in reinforced concrete [28], and monitoring ship movements after grounding [29]. In three of those publications [20,26,28] commercially available, automotive-grade MIMO-SAR systems have been used. W-Band MIMO-SAR systems were also used for deformation monitoring, but the literature focused so far on simulations [30] and close-range indoor experiments [31]. To the best of our knowledge, the use of W-Band MIMO-SAR systems to detect low-frequency deformations in the decimeter amplitude range [15] and for distances above a couple of tens of meters, as necessary for tall wind turbine towers, has not yet been demonstrated.

In this study, we used MIMO-SAR to estimate the deformation of a wind turbine tower by measuring the line-of-sight component of the displacements along a vertical section of the tower and extracting the horizontal components of the deformations therefrom. A total station and a video camera provide independent reference measurements of surface displacement at different heights of the tower (see Sections 2.2 and 2.3). These data were later used for the evaluation. Deformations were only measured for one side of the tower (approximately the north side) in this paper, but the approach can be adapted to cover also deformation components in other directions by operating several MIMO-SAR sensors simultaneously.

The main novel contribution of this paper is to empirically demonstrate the capability of automotive-grade MIMO-SAR systems for contact-less monitoring with the spatial resolution of deformations and vibrations along the height of the tower. In particular, we evaluated the performance of a Texas Instruments TIDEP-01012 [32] MIMO-SAR system for monitoring the deformations of a wind turbine's tower in Switzerland [33]; see Figure 1. It is a turbine of type *Vestas V112-3.0 MW* mounted on a tubular steel tower with a hub height of 119 m [33]. Each of the three rotor blades is 54.65 m long, rotating in an area with a diameter of 112 m [33,34]. The turbine operates when the wind speed lies between 3 and 25 m/s. Its main characteristics are summarized in Table 1.

This paper is organized as follows: First, the measurement principle and methodology of the sensors are explained (Section 2). In Section 3, the results are described and compared. This is followed by a discussion (Section 4). A summary of the findings and an outlook conclude the paper in Section 5.

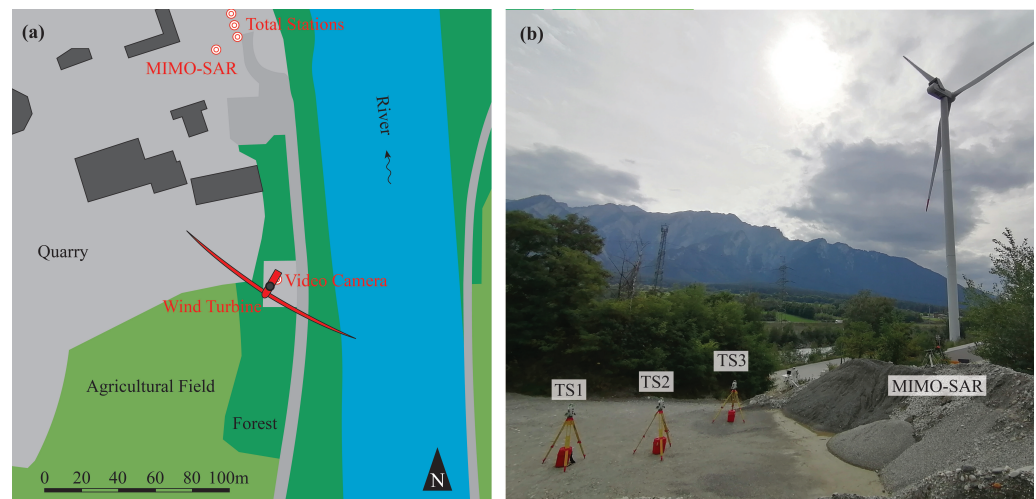


Figure 1. (a) Map with the location of the wind turbine and the measurement instruments (map based on data provided by Swisstopo). (b) Picture of the wind turbine showing the locations of the radar instrument and total stations.

Table 1. The main characteristics of the Vestas V112-3.0 MW wind turbine [33,34].

Name	Value
Number of rotor blades (-)	3
Rotor diameter (m)	112
Hub height (m)	119
Cut-in wind speed (m/s)	3
Rated wind speed (m/s)	13
Cut-out wind speed (m/s)	25
Installed capacity (MW)	3

2. Measurement Principle and Methodology

Figure 2 shows the configuration of the measurements schematically. The location of each sensor (MIMO-SAR system, total stations, and video camera) and the foundation of the wind turbine tower were determined by Real-Time Kinematic Global Navigation Satellite System (RTK-GNSS) measurements. We used coordinates in the national geodetic coordinate reference and map projection frame (Swiss CH1903+/LV95) to estimate the orientation (i.e., azimuth) of the sensors with respect to the wind turbine tower. The observed relative deformation vectors can then be separated into east–west and north–south components by utilizing the estimated azimuth of each sensor, and because all the sensors were located in the north of the wind turbine (Figure 1), only the north–south components were used for the analysis. Each sensor’s measurement principles with sample observations are described in the following Sections 2.1–2.3.

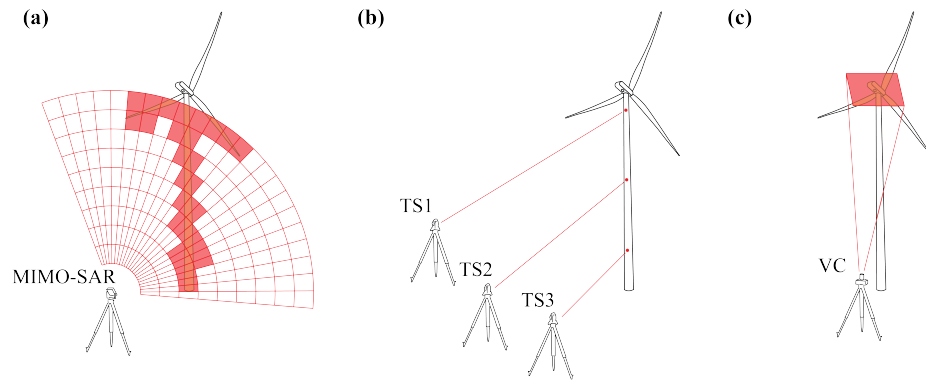


Figure 2. Illustration of the measurement arrangement for the various sensors: (a) MIMO-SAR instrument, (b) total station, and (c) video camera.

2.1. MIMO-SAR

The radar sensor used in this experimental investigation (see Figure 3a) has 12 transmitting and 16 receiving antennas creating a virtual antenna array of 86 unique antennas and resulting in an angular resolution of 1.33° at boresight. The antennas operate in the 76 to 81 GHz frequency range with a maximum configurable bandwidth $\Delta f = 4$ GHz and a range resolution $\Delta r = 3.76$ cm. The chirp parameters can be configured using the mmWave Studio software [35]. For the following investigations, we set them to the values given in Table 2. This resulted in a range resolution of 50 cm and a maximum unambiguous range of 256 m. We refer to [23] for more details regarding the general properties of MIMO-SAR systems.

Table 2. Chirp, timing, and analogue/digital conversion (ADC) parameters for the MIMO-SAR sensor.

Name	Value
Center frequency f_c (GHz)	77.2
Sweep bandwidth Δf (MHz)	300
Frequency slope s_c (MHz/ μ s)	4.973
Ramp duration T_{Ramp} (μ s)	75
Sample per chirp N_{ADC} (-)	512
ADC sampling frequency f_{ADC} (MHz)	8.493
Data acquisition rate T_{Acq} (ms)	10

The output of the MIMO-SAR instrument is a two-dimensional single-look complex (SLC) matrix for each epoch, i.e., every 10 ms. The matrix has a dimension of $m \times n$, where m is the number of bins in the cross-range direction and n is the number of bins in the range direction. Each complex number represents a superposition of signals backscattered from objects within the sensor's field of view. The signal for bin (k, l) at epoch t can be expressed as

$$SLC_t(k, l) = A_t \cdot \exp(j \cdot \phi_t) \quad \begin{cases} A_t = \sqrt{a_t^2 + b_t^2} \\ \phi_t = \arctan(\frac{b_t}{a_t}) \\ j = \sqrt{-1} \end{cases} \quad (1)$$

where a and b denote the real and imaginary parts of the complex numbers in the SLC bins, A denotes the amplitude and indicates the strength of the received signal, and ϕ denotes the complex number's phase and encodes information regarding the distance R from the radar sensor to the object. More explicitly, the relationship between them is

$$\phi_t = \frac{(2 \cdot \pi) \cdot (2 \cdot R_t)}{\lambda} \pmod{2\pi} \quad (2)$$

with λ being the wavelength of the emitted electromagnetic wave and the phase ϕ being bound to $\{\phi \in \mathbb{R} : -\pi < \phi \leq \pi\}$. Terrestrial Radar Interferometry (TRI) can then be used to detect Line-Of-Sight (LOS) displacements $\Delta R_{s,t}$ between two consecutive observations at epochs s and t . It is expressed by

$$\Delta R_{s,t} = \frac{\lambda}{4 \cdot \pi} \cdot \Delta\phi_{s,t} = \frac{\lambda}{4 \cdot \pi} \cdot (\phi_t - \phi_s) \tag{3}$$

with $\Delta\phi_{s,t}$ being the interferometric phase. Modern sensors can estimate the phase of an electromagnetic wave even in the GHz frequency range with an uncertainty of sub-degrees [36], and therefore, deformations at a fraction of the wavelength can be detected. However, deformations larger than $\lambda/4$ are ambiguous according to Equation (2) and need to be recovered using phase unwrapping [37]. Examples of interferometric amplitude and (unwrapped and scaled) phase images can be seen in Figure 4.



Figure 3. Instruments: (a) MIMO-SAR system, (b) total station, and (c) video camera.

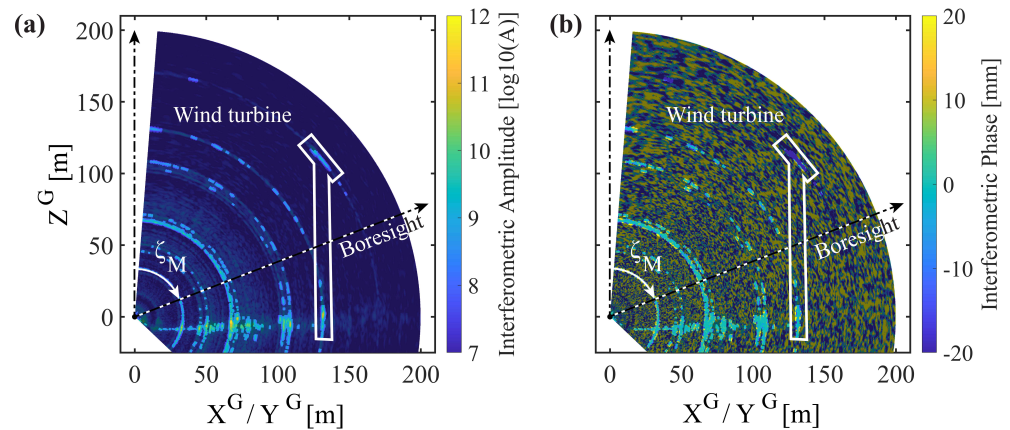


Figure 4. Example of (a) an interferometric amplitude image and (b) an interferometric phase image for a period of 30 s. For a simpler interpretation, both images are overlaid with a mask, darkening areas with coherence in a 3×3 neighborhood of less than 0.85, as well as outlining the location of the wind turbine and the direction of the antenna boresight.

In the following, we omit the time dependency of the variables ΔD and ΔR for better readability. An object’s actual deformation does not typically occur in the LOS direction. In the case of a tall object such as a wind turbine tower, the dominating deformation corresponds to height-dependent horizontal displacement of the object’s surfaces. The relationship between the LOS displacement ΔR_i of a surface point i and the horizontal component ΔD_i in the vertical plane containing the LOS (i.e., in the same azimuthal direction as the LOS displacement) can be expressed by

$$\Delta D_i = \Delta R_i \cdot \sin \zeta_i \tag{4}$$

with ζ_i being the zenith angle between the radar instrument and the surface point i , as can be seen from Figure 5.

The zenith angle can be calculated by (i) resolving the bin's angular deviation θ_i from the MIMO-SAR's boresight [38] and (ii) by measuring the zenith angle ζ_M of the instrument after its setup by using an inclinometer or other suitable measurement procedures or by reconstructing it from the amplitude images. In the next step, the horizontal deformations ΔD_i are split into east–west (Y^G) and north–south (X^G) components to bring all observations to a common coordinate reference system, based on the azimuth:

$$\alpha_i = \arctan\left(\frac{X_i^G - X_M^G}{Y_i^G - Y_M^G}\right) \quad (5)$$

of the monitored point with respect to the location of the instrument. Here, the coordinates of the instruments are denoted as $P_M = [Y_M^G \ X_M^G]^T$, and the coordinates of the object point (strictly speaking, of the point in space corresponding to the bin center) are denoted as $P_i = [Y_i^G \ X_i^G]^T$. However, since we evaluated the displacement of points within a vertical plane only, and set up the MIMO-SAR instrument accordingly, all points i have the same azimuth $\alpha_i = \alpha$. We determined α from the coordinates of the turbine tower and the radar instrument using RTK-GNSS. The components are then calculated by

$$\begin{bmatrix} \Delta D_{Y_i^G} \\ \Delta D_{X_i^G} \end{bmatrix} = \begin{bmatrix} \cos \alpha_i \\ \sin \alpha_i \end{bmatrix} \cdot \Delta D_i. \quad (6)$$

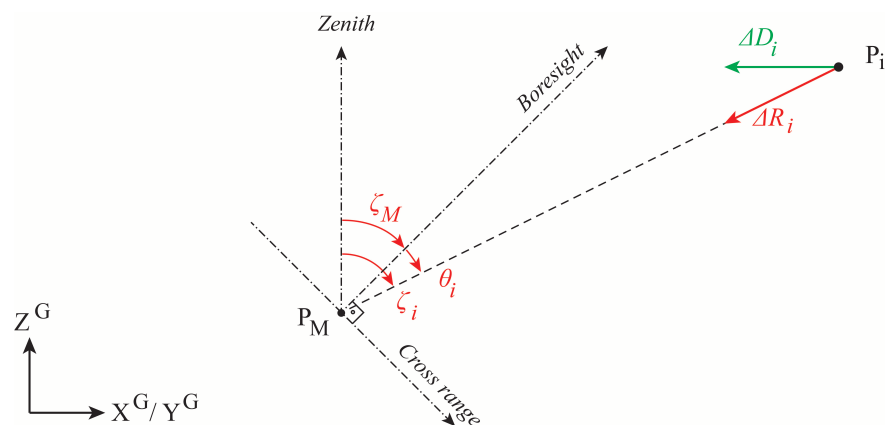


Figure 5. A vertical cross-section of the acquisition geometry showing the definition of the local coordinate system of a MIMO-SAR system with its relation to the three-dimensional global coordinate system. P_M denotes the location of the MIMO-SAR sensor. The sensor's boresight is tilted by an angle ζ_M with respect to the zenith direction. The target object at location P_i is at a slope distance R_i in a direction deviating from the boresight by the cross-range angle θ_i .

2.2. Total Station

We used three Leica Geosystems TS60 total stations (see Figure 3b) to obtain reference measurements of the wind turbine deformations. They were set up on tripods in close proximity to the MIMO-SAR system, about 135–145 m north of the wind turbine tower; see Figure 1. The three total stations were targeted in the direction of the tower at heights of 39, 78, and 115 m above the ground, which correspond to the heights of two distinct features on the surface of the tower, visible also in the camera images, and to the tower right below the nacelle. The total stations measured the distance in a so-called reflector-less mode in the fixed directions given by their setup. These distance measurements were obtained with a data rate of 0.8 to 1.5 Hz (constant time intervals cannot be enforced with these instruments) and, according to the specification of the instruments, with a standard deviation of about 2 mm. The total stations were not moved and carried out measurements over the whole duration of the experimental investigations. Therefore,

the zenith angles output by the instruments were averaged for each station over the whole measurement period of approximately 2 h, giving $\bar{\zeta}$. The slope distance measurements were also averaged over the whole period giving \bar{R} . The horizontal deformation ΔD over time was calculated by

$$\Delta D_i = (R_i - \bar{R}) \cdot \sin(\bar{\zeta}) \quad (7)$$

The east–west and north–south components in the global coordinate system can then be derived by (i) calculating the azimuth of the total stations using Equation (5), again using the RTK-GNSS measurements, and (ii) afterwards, applying Equation (6).

2.3. Video Camera

The third instrument used for observing deformations was a camera. This approach was already used in [15]. In our experiment, we used a *Nikon D5500* with a zoom lens kept at a constant focal length throughout the experiment (Figure 3c). The camera was mounted on a tripod and located at the bottom of the tower looking upward. It was programmed to record an image every 0.04 s and, thus, resulted in a video stream showing the bottom of the turbine’s nacelle. Figure 6 shows (a) the camera’s location and (b) a sample frame with the bottom of the nacelle and some features (e.g., screws, covers, etc.), as well as various sensors attached to the tower. It can be assumed that the resulting frames were already orthorectified due to the large distance (>100 m) and the orthogonal setup (located at 90°) of the camera concerning the observed surface of the nacelle. We used the MATLAB software with the function `detectMinEigenFeatures` to detect features and track them automatically over all video frames using the point tracker method `MaxBidirectionalError`. The coordinates of the features in the image coordinate system (pixels) originated in the frames’ top-left corner. Those coordinates were inverted to be originating on the lower-right corner of the frame and scaled by a factor s to a metric system using the known width of the nacelle and the size of the various sensors visible in the video frames (Figure 6):

$$\begin{bmatrix} Y^{Ci} \\ X^{Ci} \end{bmatrix} = s \cdot \begin{bmatrix} 1920 - Y^C \\ 1080 - X^C \end{bmatrix} \quad (8)$$

The scale factor s introduces uncertainty to the coordinate transformation, which relies on the size of the known object used for scaling. Being just one pixel off by defining the size of the object in the image will introduce an error of 2.6 (3.1 mm/px), 5.2 (6.2 mm/px), and 0.2% (7.4 mm/px) at the heights of 38, 78, and 120 m, respectively. Afterwards, the coordinates were rotated, so the axes were parallel to the previously defined global reference system. This operation can be expressed by

$$\begin{bmatrix} Y_k^G \\ X_k^G \end{bmatrix} = \begin{bmatrix} \cos \alpha & -\sin \alpha \\ \sin \alpha & \cos \alpha \end{bmatrix} \cdot \begin{bmatrix} Y_k^{Ci} \\ X_k^{Ci} \end{bmatrix} \quad (9)$$

with k indicating the index of a pixel in the image frame and α being the azimuth value of the camera frame (Figure 6) derived from Equation (5) in combination with GNSS measurements at the location of the camera. The occurring deformations separated into their east–west and north–south components can then be determined by

$$\begin{bmatrix} \Delta D_{Y_k^G} \\ \Delta D_{X_k^G} \end{bmatrix} = \begin{bmatrix} Y_k^G \\ X_k^G \end{bmatrix} - \begin{bmatrix} \overline{Y_k^G} \\ \overline{X_k^G} \end{bmatrix} \quad (10)$$

with $\overline{Y_k^G}$ and $\overline{X_k^G}$ being the average position over the time series. Applying this procedure to feature points determined at the meteorological sensors mounted on the tower (Figure 7) will give comparable results as for the measurements acquired with the radar instrument and total stations. The wind turbine’s nacelle changes its direction along with the direction of the wind. The movements of the tracked features (see Figure 7, yellow cross) would, therefore, not be representative of the movement of the tower if the rotation

of the nacelle were not accounted for. The tower’s movement can be estimated by adding two intermediate steps to determine the estimated center of the tower on the height of the nacelle:

1. Calculating the transformation parameters of the tracked feature points: The transformation matrix \mathbf{T} describes the relationship between the initial position of all the tracked features at time t_0 with the position of all features at time t_i and can be described by

$$\underbrace{\mathbf{C}_{t_i}^G}_{(2 \times n)} = \underbrace{\mathbf{T}}_{(2 \times 2)} \cdot \underbrace{\mathbf{C}_{t_0}^G}_{(2 \times n)} \tag{11}$$

with \mathbf{C}^G containing a list of coordinates $[\mathbf{Y}^G \ \mathbf{X}^G]^T$ for feature points at a given time. This linear equation requires at least two independent feature points to be solved. Having more points leads to an over-determined equation system, and a least-squares adjustment [39,40] was performed to obtain a unique solution for \mathbf{T} .

2. Estimating the center coordinate of the tower: The video frames clearly show some parts of the cylindrical tower’s surface at the height of the nacelle (Figure 7). The first frame was used to manually select a set of points on the tower’s surface. The position of the tower’s surface for each frame was derived by applying Equation (11) and using the previously derived transformation matrix \mathbf{T} . The tower’s center was then estimated for each frame by solving the standard equation for a circle:

$$(x - u)^2 + (y - v)^2 = r^2 \tag{12}$$

with x and y representing coordinates on the circle, u and v representing the coordinates of the circle center, and r being the radius of the circle. Again, a least-squares adjustment for each frame was carried out to obtain a unique solution for the center coordinate. Those center coordinates will then be used as the input for Equation (9) to determine the east–west and north–south components based on Equation (10).

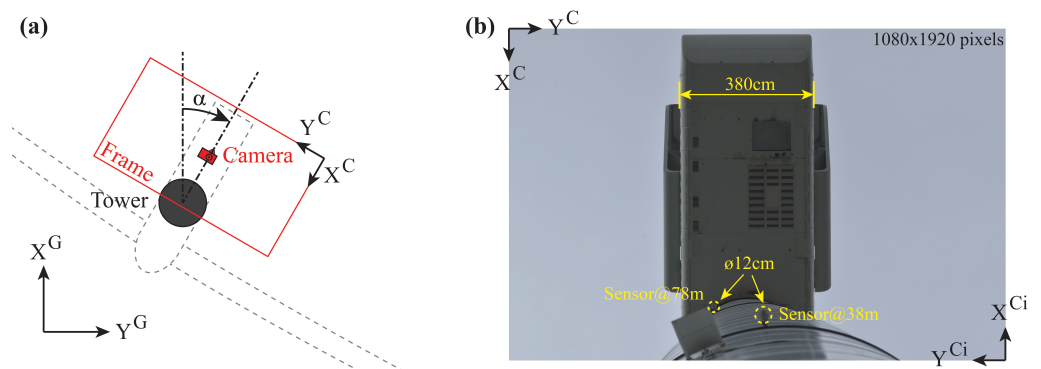


Figure 6. Example of (a) the camera setup with the respective coordinate systems and (b) a sample frame with annotations, where the two sensors firmly mounted on the tower are outlined with circles.

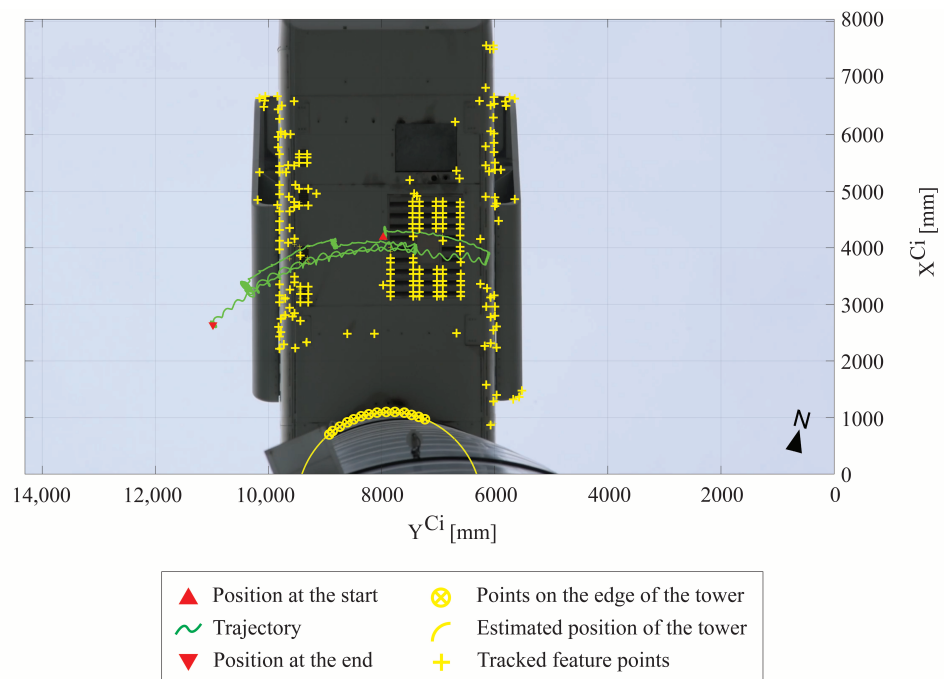


Figure 7. Example of the feature point tracking of the video recording. The image of the first recorded frame is overlaid with yellow crosses (+) and circles (o). The first ones are the automatically detected feature points, while the latter ones are the manually selected points on the intersection between the tower and the nacelle. The green line shows the trajectory derived over the period of 20 min for the nacelle.

3. Results

The following subsections describe the results of the investigations. First, we show in Section 3.1 the stability index for filtering the MIMO-SAR acquisitions. This is followed in Section 3.2 by the results for the deformation measurements for all three sensors, as well as the frequency analysis of the same in Section 3.3.

3.1. MIMO-SAR Data Filtering

The MIMO-SAR system observes an extensive area visualized in Figure 4. The radar instrument returns an SLC image, where a bin at every position in the FOV contains information. However, only bins representing physical objects with a reflected signal strong enough to be detected are useful. Statistical filtering is helpful to clean the data and only keep bins representing persistent scatterers. For this work, we used a two-step approach to select persistent scatterers. (i) We reduced the total amount of data by defining a polygon enclosing the region of bins, which represent the wind turbine. (ii) We applied a filter to select persistent scatterers based on two indices. The first index is based on the amplitude value of a bin, named the Amplitude Stability Index (ASI) [41]:

$$\text{ASI} = 1 - \frac{\sigma_{\text{AMP}}}{\overline{\text{AMP}}} \quad (13)$$

with σ_{AMP} being the standard deviation of the amplitude over time for a single bin and $\overline{\text{AMP}}$ being the average of the amplitude for the same bin. The second index is based on the coherence [42] of an SLC bin in its 3×3 spatial neighborhood, named the Coherence Stability Index (CSI), defined by

$$\text{CSI} = 1 - \frac{\sigma_{\text{COH}}}{\overline{\text{COH}}} \quad (14)$$

with $\overline{\text{COH}}$ being the average over time of the coherence of a bin and σ_{COH} being the standard deviation of the coherence over time. We combined these indices by multiplying them, creating the Stability Index (SI) as

$$\text{SI} = \text{ASI} \cdot \text{CSI} \tag{15}$$

with $\text{SI} \in [-\infty, 1]$, where a value close to 1 indicates a persistent scatterer, while lower values indicate lower-quality scatterers or noise. Figure 8 shows the SI for a time series of MIMO-SAR acquisitions. The SI image shows multiple circular patterns also visible in Figure 4 caused by side lobes of strongly reflecting objects. The location of the turbine tower and turbine/blades can be recognized when looking at the zoom-in in Figure 8b. The origin of the $X^G Y^G Z^G$ system is set to be the center of the MIMO-SAR system. A section of the turbine tower is visible in this SI image as a vertical line from approximately $Z^G = -9$ m to 40 m at a horizontal distance of 130 m. The tower is then not recognizable anymore at $Z^G = 40$ m and above. The turbine nacelle gives a higher SI again at about $Z^G = 110$ m. For the following analysis, we selected four bins at heights of 9, 38, 78, and 120 m above ground, coinciding with the locations of the observations carried out with the other sensors. At each height, we only processed the bin with the highest SI value within a small neighborhood (a few square meters) of the corresponding location, with the SI values being in the range of 0.31 (at height 78 m) to 0.9 (at height 9 m).

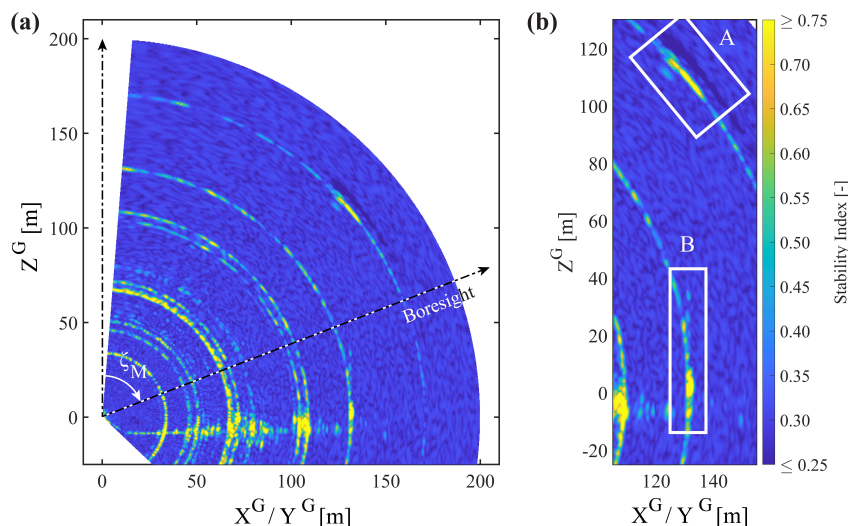


Figure 8. Example of stability indices for a time series of MIMO-SAR acquisitions over a period of 30 s with (a) showing the same section as in Figure 4 and (b) being a detailed view of the wind turbine where the turbine and top of the tower are outlined with a box A, and the lower third of the tower is outlined with a box B.

3.2. Deformations

Figure 9 shows the deformation component ΔD_{X^G} independently derived from the observations of the three sensor systems for areas with sufficiently high SI to allow radar-based deformation monitoring. Deformations between -2 and 2 mm were observed at the tower height of 9 m and between -50 and 50 cm at the towers' top. The processing of the video camera and total station data resulted in similar deformation patterns for the same area. However, the deformations derived from the total station measurements were typically smaller than those observed with the video camera. This can be related to the different information content of the respective measurements: the total stations measured the distance change of the tower's surface in a specific, fixed spatial direction, while the camera results provide the displacement of specific surface points on the tower. Therefore, depending on the actual direction of movement of the tower, not the same

target is measured with the different technologies. This effect is displayed in Figure 10a, where the horizontal deformations in ΔD_{X^G} are visualized for the tower at the height of 120 m and a period of 100 s starting with epoch $t = 314$ s (zoom-in of Figure 9a). In this period, the bias E between the deformations derived from the video camera recordings and the total stations reached values of up to 23.5 cm. In Figure 10b, we display the horizontal movements derived from the video camera recordings for the same period. During this period, the top part of the tower moved towards north–east by about 1 m. The total station aimed at the tower with a constant azimuth angle of about 172° . The LOS displacement ΔD_{LOS}^{TS} and the corresponding coordinate change in the direction of X^G derived from the total station measurements are, therefore, different from the LOS or the X^G component of the actual displacement of the tower's top center, which is reflected by the displacement estimates ΔD_{LOS}^{VC} and $\Delta D_{X^G}^{VC}$ obtained from the camera. Assuming that, by coincidence, the total station's LOS direction points exactly towards the center of the tower at $t = 314$ s, the maximum bias between the total station and camera results would be 21 cm. This coincides very well with the previously mentioned bias E derived from the actual observations. However, the discrepancy between the LOS direction and the direction to the center of the tower is not known with sufficient accuracy from the instrument setups for compensating the apparent bias between the camera and the total station results.

The MIMO-SAR system has been able to derive displacements up to a distance of about 175 m from the sensor's location. This is further away than the maximum range of 150 m mentioned in the sensor specification [32] for a target with a radar cross-section of 10 m^2 . We selected the bins for the following analysis carefully and chose points at the extension of the tower direction, as visible in the lower third of the tower (e.g., white box notated with B in Figure 8b). At the turbine's height (Figure 9a), the deformations coincide partially with the deformation observed with the other two sensor types, and sometimes, the deformations show a difference with the other two sensor types. These transitions coincide with the times when the turbine nacelle rotated, which are indicated by grey backgrounds in Figure 9. The rotations contaminate the (apparent) LOS displacements for some radar bins by the radar layover effects (where parts of the nacelle and of the tower may mix into the data of the same bin). The georeferencing of the radar data were not accurate enough in the present experiment to clearly distinguish between the top of the tower and the nacelle in the present experiment, so the analyzed bin could represent an area on the turbine nacelle and not on the tower itself.

Furthermore, the MIMO-SAR system did not measure constantly, but started every 240 s a new set of acquisitions with an acquisition gap of a few seconds; see Figure 9. The acquisition gaps are attributable to the system properties of the MIMO-SAR system used in this experiment, as it does not assign temporal information (i.e., time stamps) to the acquisition and can only store a limited number of continuous measurements at a time ($N_{\max} = 65'535$ SLCs [20]). Therefore, we decided that the acquisition set consisted of up to 23'600 SLCs and took up to 236 s. A new set was then initiated after a break of 4 s. Periods without observations are prone to cause phase unwrapping errors and potentially introduce a bias in the derived deformations for the period after the data gap. This effect can be seen in Figure 9b, where the data gaps in the seconds before 240, 480, and 720 s cause an offset of the MIMO-SAR results as compared to the VC and TS results. Based on their agreement, we considered the latter to be more reliable. We attributed the MIMO-SAR deviations to phase unwrapping errors. This offset or phase unwrapping error occurred as soon as the displacement between two consecutive radar acquisitions exceeded a quarter of the wavelength (i.e., 0.95 mm for W-Band MIMO-SAR) and can reach any value. Further investigations using MIMO-SAR hardware without the data gap problem will be needed to clarify whether there are further reasons for the drift of the results.

In Figure 9c, the deformations of the tower at a 9 m height are displayed. Reference measurements for this location do not exist. However, the detected movements have the same deformation pattern as derived from the video camera for the other heights.

Furthermore, the deformations at a 9 m height range from -2 to 2 mm and are reasonable, since this area is located near the foundation where deformations should be close to zero.

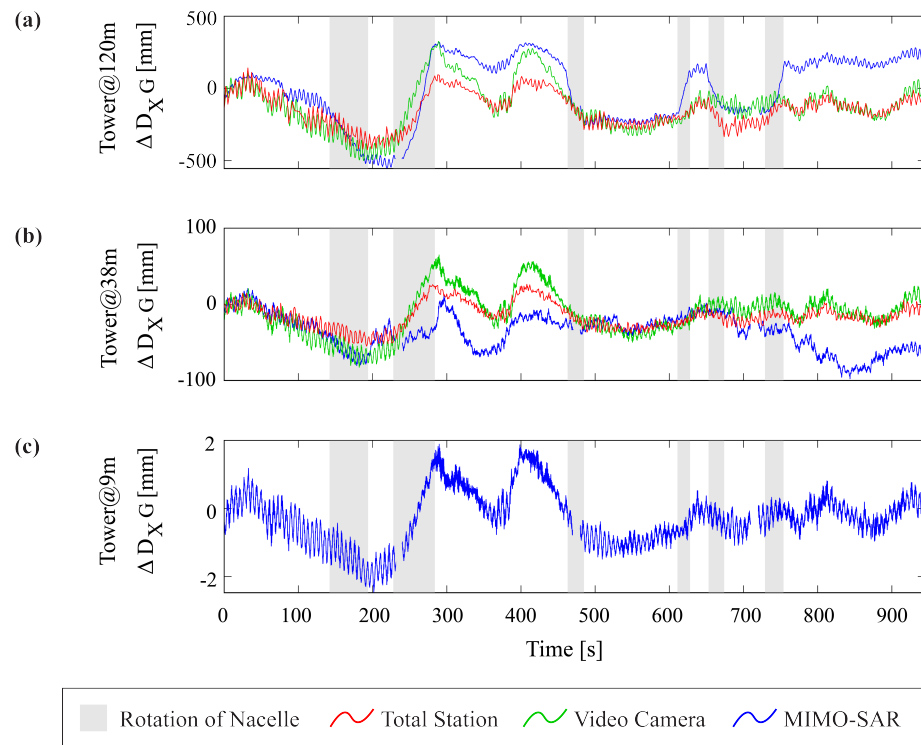


Figure 9. Deformation ΔD_{XG} of the wind turbine tower at heights of (a) 120, (b) 38, and (c) 9 m above the ground.

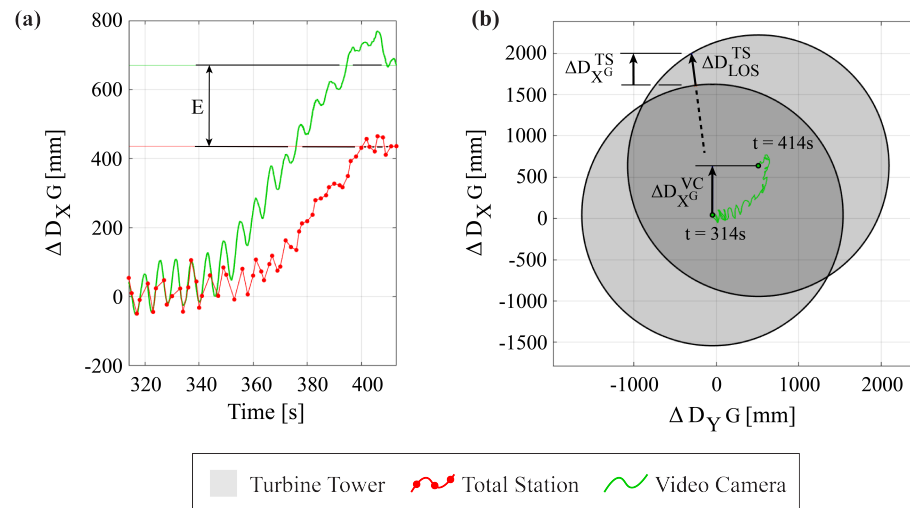


Figure 10. Deformation of the wind turbine tower occurring at a height of 120 m for a period of 100 s starting with epoch $t = 314$ s (zoom-in of Figure 9a). (a) Deformation ΔD_{XG} over time. (b) Location and diameter of the wind turbine tower at epochs $t = 314$ s and $t = 414$ s estimated from the video camera recording.

The interferometric amplitudes of the MIMO-SAR acquisitions were, unfortunately, very low for the area at a height of about 78 m, and it is not easy to recognize the bins representing the tower. The bin with the highest SI value ($SI = 0.31$) within this area was selected. In Figure 11, the deformations derived for all sensors are visualized. The deformation derived from the total station and video camera recording coincide with each other,

but the deformations derived from the MIMO-SAR acquisitions do not at all. These invalid deformation measurements are the result of the weak amplitude signal. The strength of the received signal depends on various observation properties, e.g., the measurement distance to and the Radar Cross-Section (RCS) of the target [43]. The distance is similar for all the analyzed bins and does not explain the low amplitude. However, the RCS of a smooth, cylindrical surface decreases with a steeper Angle Of Incidence (AOI) ([44], p. 35) and explains the lower amplitude of the bin at 78 m (AOI of approximately 30°) compared to the bins at 9 m (AOI of approximately 0°) and 38 m (AOI of approximately 15°).

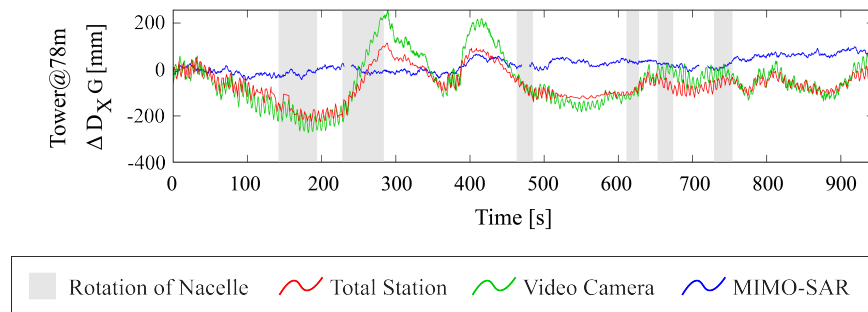


Figure 11. Deformation ΔD_{XG} of the wind turbine tower at heights of 78 m above the ground.

To assess the uncertainty of the measurements, we aimed to estimate the noise of the data. The wind turbine tower constantly moves in a range exceeding the wavelength of the emitted electromagnetic wave (3.8 mm). Therefore, the common standard deviation cannot be used to quantify the noise without data manipulation (i.e., detrending the time series). The Allan deviation is invariant to constant biases and linear drifts [45]. It is typically used for assessing the accuracy of sensors (e.g., IMU, clocks) whose noise increases over time. The noise of MIMO-SAR observations does not increase with time, but the deformation measurements of a moving object can cause an apparent increase in noise over time. It can, therefore, be advantageous to use the Allan deviation also for time series of deformation measurements. It is calculated by

$$\sigma_{\text{Allan}}(\tau) = \sqrt{\frac{1}{2} \cdot \langle (\bar{y}_{n+1} - \bar{y}_n)^2 \rangle} \quad (16)$$

with \bar{y} denoting the averaged deformation over the n-th observation period of duration τ and $\langle \cdot \rangle$ denoting the expectation operator. We calculated for every bin in the tower's vicinity the Allan deviation σ_{Allan} and display the results in Figure 12. The vertical axis represents the resulting Allan deviation for $\tau = 0.01$ s, i.e., for an individual measurement, and the horizontal axes represent the Stability Index (SI) and the amplitude. Weak (low amplitudes) and not very stable (low SI) signals have high Allan deviations with a few hundred micrometers. The bin at about 78 m above the ground located about 150 m from the MIMO-SAR sensor has an Allan deviation for individual measurements of 313 μm . It is also at the border of the rectangularly arranged dots representing bins in physically empty space or of targets with low sensitivity to the emitted wavelength or a small RCS. This shows that the selected bin at the height of about 78 m is not representative of the actual deformation of the tower at this location.

The bins representing the tower at heights of 9, 38, and 120 m are also highlighted in Figure 12. Combined with the distribution of the other bins in the vicinity of the tower, it can be seen that the higher the SI or amplitude value is, the smaller the noise represented by the Allan deviation is. The bin at the height of 9 m has a very low Allan deviation of just 13 μm , while the bins at 38 and 120 m have a relatively high Allan deviation of 249 and 231 μm , respectively. In Figure 12c are the Allan deviations of the bins with an $\text{SI} \geq 0.31$ visualized. Mostly bins at the lower third of the tower remain with a prominent circularly

arranged set of bins caused by side-lobes of the very strong reflection of the tower at the height of about 9 m, as well as a few bins at the top of the tower in the vicinity of the turbine.

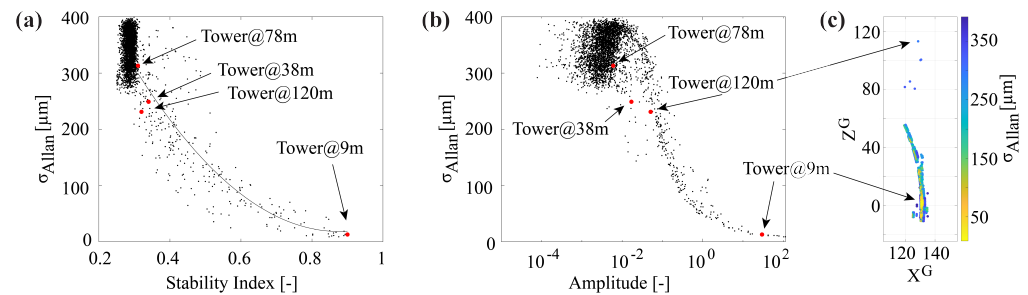


Figure 12. Visualization of bins in the vicinity of the turbine tower for MIMO-SAR acquisitions over a period of 945 s with (a) showing the Allan deviation versus the stability index, (b) showing the Allan deviation versus the amplitude, and (c) showing the bins with an $SI \geq 0.31$ in the global coordinate system.

3.3. Frequencies

The deformation time series in Figure 9 show an oscillation. Looking closely at an excerpt of such a time series (Figure 13a–c), the slowly oscillating movements with a periodicity of a few seconds can be seen for all three sensors. However, the video camera (Figure 13b) and MIMO-SAR (Figure 13c) acquisitions show additional faster vibrations due to the higher data acquisition frequency of 25 and 100 Hz, respectively. Applying a Fourier transform gives the frequencies and amplitudes of the deformation of the tower. For the following analysis, the data acquired by the total station were not processed due to the irregular and slow sampling frequencies of less than 1 Hz, as seen in Figure 13a. Figure 14 shows the result of the Fourier transform for the video camera and MIMO-SAR acquisitions. Six frequencies can be identified by the video camera, with the predominant ones being at 0.169 Hz (No. 1) and 1.304 Hz (No. 4). The same frequencies are also dominant for the MIMO-SAR acquisition with 0.167 Hz (No. 1) and 1.291 Hz (No. 4). Those frequencies deviate from the ones derived from the video camera by -1.2% and -1% , respectively. However, Frequency Nos. 2, 5, and 6 are not recognizable. When also performing the Fourier transform for the MIMO-SAR acquisition at the height of 9 m above the ground (Figure 15), then all frequencies can be seen. When comparing them again, then they deviate between 0.6 and 2.4%. However, because of the high acquisition frequency of 100 Hz for the MIMO-SAR system, in combination with uncertainties in the deformation measurement in the sub-mm range, five additional frequencies can be seen with values up to 23.974 Hz. An overview of all detected frequencies is given in Table 3.

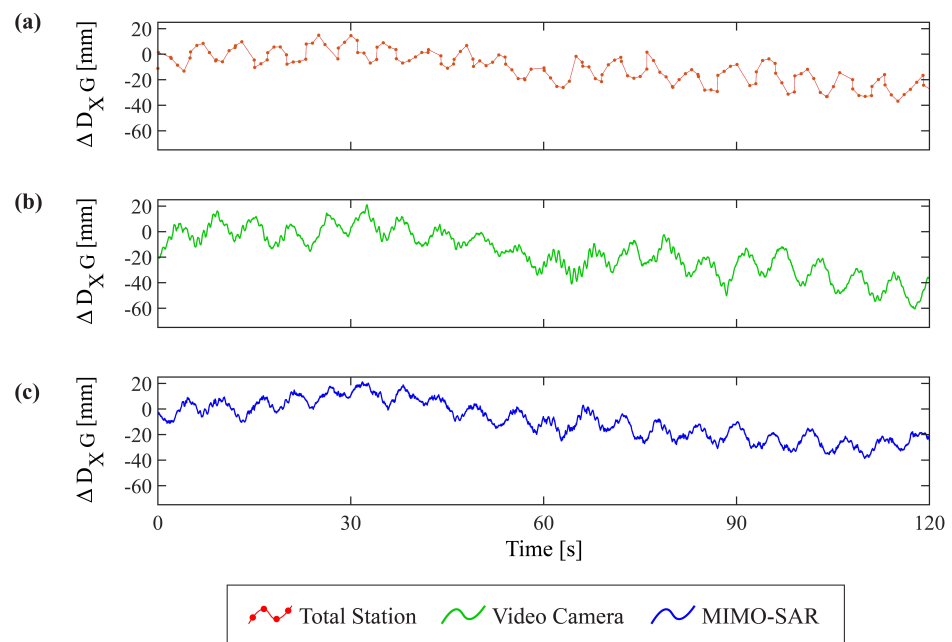


Figure 13. Deformation ΔD_{XG} of the tower at the height of the sensor at 38 m above the ground derived from (a) total station, (b) video camera, and (c) MIMO-SAR acquisitions.

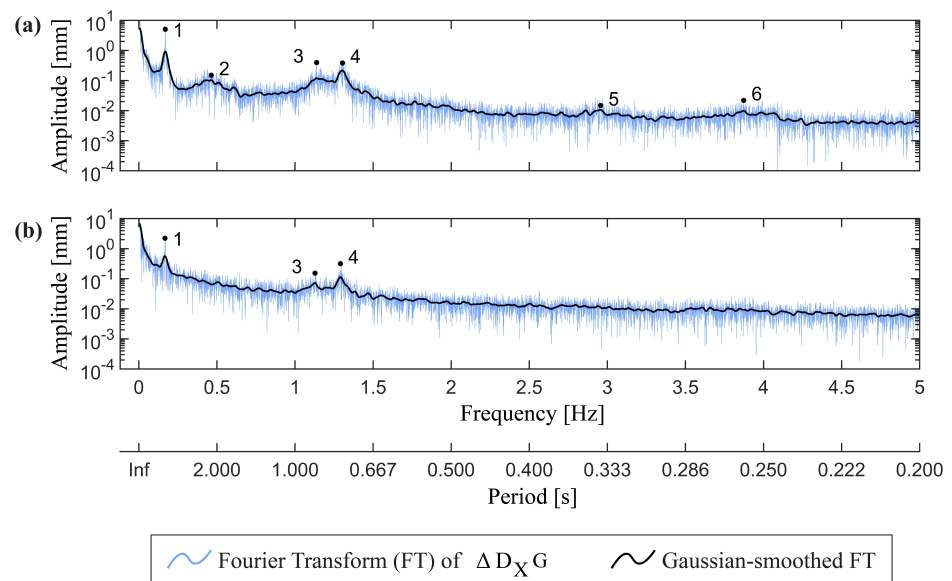


Figure 14. Fourier transform of the tower movement ΔD_{XG} at the height of 38 m above the ground as derived from (a) video camera and (b) MIMO-SAR acquisitions for the frequency range between 0 and 5 Hz.

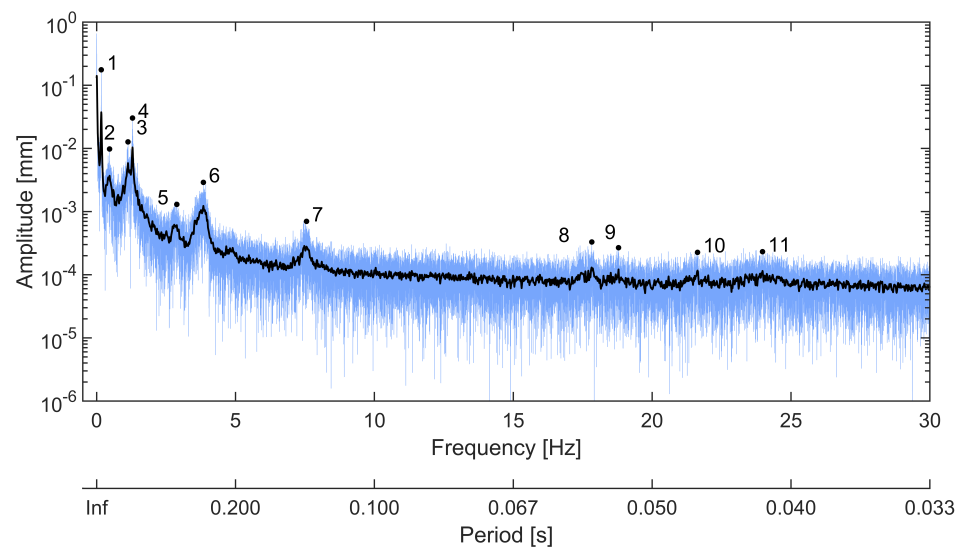


Figure 15. Fourier transform of the tower movement $\Delta D_{\chi G}$ at a height of 9 m above the ground as derived from MIMO-SAR acquisitions for the frequency range between 0 and 30 Hz.

Table 3. Deformation frequencies of the wind turbine tower.

Name		Frequency (Hz)										
		1	2	3	4	5	6	7	8	9	10	11
Video Camera	Tower@38m	0.169	0.463	1.138	1.304	2.957	3.873	-	-	-	-	-
MIMO-SAR System	Tower@38m	0.167	-	1.128	1.291	-	-	-	-	-	-	-
MIMO-SAR System	Tower@9m	0.167	0.466	1.129	1.292	2.887	3.844	7.557	17.822	18.790	21.634	23.974

4. Discussion

We measured the deformation of a wind turbine tower occurring under load. The bins representing the wind turbine tower were located at distances between 130 m and 175 m from the position of the MIMO-SAR sensor.

For the assessment, we had to filter the MIMO-SAR acquisitions to only keep bins representing persistent scatterers, which could contain useful measurements. For this aim, we introduced a Stability Index (SI) consisting of a combination of the Amplitude Stability Index (ASI) and the Coherence Stability Index (CSI) and calculated it for each bin in the vicinity of the wind turbine. We compared the SI value with the Allan deviation for each bin and showed that the persistent scatterers in this experiment have an SI value of more than 0.31 and an Allan deviation smaller than 250 μm . Some of the analyzed bins at distances of about 130 m had Allan deviations in the region of 10 μm , if the corresponding bins had SI values of about 0.9. This analysis also showed that most persistent scatterers were located in the lower third of the tower (i.e., up to a height of 40 m), with a few more being at the top at the junction between the wind turbine nacelle and the tower (i.e., at a height of 120 m).

The deformations derived from the total station acquisitions and video camera recording were considered as the ground truth. Those deformations were compared quantitatively with a subset of the radar bins. For the comparison, we could not separate the influence of the methods and sensors, but assessed the accuracy as a combination of both. For the bin located the farthest from the MIMO-SAR sensor and representing the tower at a height of about 120 m, the derived deformations corresponded well with the other sensors as long as the turbine nacelle was not rotating to align again with the direction of the wind. The rotation of the nacelle caused a bias in the deformation measurements, indicating that the analyzed bin was not exclusively covering the wind turbine tower, but at least partially covering also an area of the nacelle. For the bin representing the tower at a height of about 38 m, the corresponding deformation patterns were visible. However, the MIMO-SAR sensor was not acquiring data constantly, but had interruptions of a few seconds every four

minutes. Deformations occurring in this time frame caused phase unwrapping errors and also introduced a bias in the following deformation measurements.

Generally, the deformation of a smooth metallic object like a wind turbine tower can be measured with the W-Band MIMO-SAR at distances exceeding 100 m with sub-mm accuracy. However, measuring displacements were not possible at every location along the tower. A target reflects the strongest signal if the emitted electromagnetic wave arrives at the target with an angle of incidence of 0° (normal to the surface), e.g., [20]. The signal deteriorates with increasing angle of incidences and is, in the case of the wind turbine tower, lost in the noise at about 15° and preventing the acquisition of useful observations. The nacelle of the wind turbine itself creates a corner-cube-like structure. This results in a strong reflectance allowing displacement measurements in slope distances of 175 m and at height of 120 m above the ground.

Furthermore, we derived the vibration frequencies and could show that the MIMO-SAR sensor obtained dominant frequencies from the deformation measurements between 0.169 Hz and 23.974 Hz. The frequencies up to 3.844 Hz were compared with the ones derived from the video camera recording, and they deviated between 0.6 and 2.4%. The MIMO-SAR system used in this investigation acquired data with an acquisition rate of 100 Hz and would therefore be able to detect vibrations with a frequency of up to 50 Hz. However, it was shown in [20] that this MIMO-SAR system can acquire data with an acquisition rate of up to 800 Hz, indicating the capability to detect vibration frequencies of up to 400 Hz. Relevant for the detectability of vibration with this MIMO-SAR system is, next to the previously mentioned temporal component, also the spatial component. The amplitude of the vibration needs to exceed the sensor noise to be detectable. However, the noise depends mainly on the target property and can not be generalized for all cases, as seen above.

5. Conclusions

The goal of this investigation was to show the capabilities and limitations of MIMO-SAR sensors operating in the W-band frequency for applications in structural health monitoring. More specifically, we investigated the feasibility of using a low-cost W-band MIMO-SAR sensor to measure centimeters to meter deformations of high structures in the example of a wind turbine tower.

We showed that the MIMO-SAR sensor could observe deformations up to a slope distance of about 175 m, which is even further away than the maximum range of 150 m mentioned in the sensor specification [32]. Due to the fast acquisition frequency, we could successfully phase unwrap the interferometric measurement and observe deformations exceeding the threshold of $\lambda/4$ or 0.95 mm. In fact, we could observe deformations in the range of up to 1 m even exceeding the configured range resolution of 0.5 m. However, we saw that the rotation of the wind turbine nacelle, which aligns the rotors with the direction of the wind, affects the measurements and would need to be taken into account and filtered out for an accurate estimation of the towers' deformation from the radar data.

The vibration frequencies of the tower were studied. The MIMO-SAR sensor identified the towers' dominant frequencies (0.169, 1.138, and 1.304 Hz) at a height of 38 m above the ground, which differed from those estimated by the video camera by only around 1%. The MIMO-SAR sensor was used to derive the deformation of the tower at the height of about 9 m above the ground. There, a total of eleven natural frequencies ranging up to 23.974 Hz were identified.

Overall, the shown results indicate that the MIMO-SAR can measure deformations of a smooth and metallic wind turbine tower up to an angle of incidence of 14.5° for a tower located at distances of about 130 m. At higher incidence angles, only corner-like structures (e.g., at the turbine's nacelle) create a strong enough signal for reliable deformation measurements. The experimental investigation showed that the MIMO-SAR systems used in this investigation still has some weaknesses (e.g., temporal gap between sets of acquisitions, association of bins to actual objects) and that for real-case

applications, it is recommended to use an independent measurement sensor for evaluating the observations. Nevertheless, the MIMO-SAR system showed its strengths compared to other sensors typically used in SHM. The sensor is a low-cost (i.e., USD ~3500) sensor with the ability to acquire data within a short time period (~hour) and without the need to directly access the site and install in situ sensors (e.g., strain gauges or accelerometers) or targets for remote sensing devices (e.g., photogrammetry or laser scanning). Furthermore, MIMO-SAR systems generate two-dimensional displacement maps and can achieve sub-mm accuracy for deformation measurements on targets with high amplitudes. This allows observing very small displacements at different heights of the target and, therefore, the verification of model assumption, as well as independent control of measurements acquired by in situ sensors installed in the (upper area) of the tower.

Currently, we have only used one MIMO-SAR sensor to derive the line-of-sight deformations of the wind turbine tower, thus proving that the MIMO-SAR is generally suitable for deriving relevant parameters (i.e., vibration frequencies) for structural health monitoring of tall wind turbine towers. Future research could involve (i) investigating the influence of the angle of incidence on a smooth cylindrical surface onto the measurement uncertainties, (ii) assessing the temporal accuracy of the MIMO-SAR sensor by comparing it with highly accurate sensors (i.e., accelerometers) or well-known target vibrations (i.e., vibration calibrator), and (iii) using three or more simultaneously operating MIMO-SAR sensors to derive actual three-dimensional deformation vectors of the wind turbine tower while simultaneously acquiring data regarding the direction of the wind and the yaw angle of the turbine for the interpretation of the deformation.

Author Contributions: Conceptualization, A.B.-O., J.A.B. and A.W.; formal analysis, A.B.-O.; investigation, A.B.-O.; methodology, A.B.-O.; software, A.B.-O.; supervision, A.W.; visualization, A.B.-O.; writing—original draft, A.B.-O.; writing—review and editing, A.B.-O., J.A.B., M.V. and A.W. All authors have read and agreed to the published version of the manuscript.

Funding: This research received no external funding.

Data Availability Statement: The data underlying this study are available upon request. The source code for data processing is available under an open-source license at <https://github.com/abgbaumann/MIMO-SAR> (accessed on 2 January 2023).

Acknowledgments: We thank Thomas Posur, ETH Zürich, for the technical support and help with carrying out the experiments.

Conflicts of Interest: The authors declare no conflict of interest.

Abbreviations

The following abbreviations are used in this manuscript:

ADC	Analog-to-Digital Converter
AOI	Angle Of Incidence
FMCW	Frequency-Modulated Continuous Wave
FOV	Field Of View
GNSS	Global Navigation Satellite System
LOS	Line-Of-Sight
MIMO	Multiple-Input Multiple-Output
Radar	Radio detection and ranging
RAR	Real Aperture Radar
RCS	Radar Cross-Section
SAR	Synthetic Aperture Radar
SHM	Structural Health Monitoring
SLC	Single-Look Complex
TI	Texas Instruments
TRI	Terrestrial Radar Interferometry
TS	Total Station
VC	Video Camera

References

1. BP p.l.c. *BP Statistical Review of World Energy 2022*; Technical Report; 2022. Available online: <https://www.bp.com/content/dam/bp/business-sites/en/global/corporate/pdfs/energy-economics/statistical-review/bp-stats-review-2022-full-report.pdf> (accessed on 1 January 2023).
2. Wisler, R.; Bolinger, M.; Hoen, B.; Millstein, D.; Rand, J.; Barbose, G.; Darghouth, N.; Gorman, W.; Jeong, S.; Paulos, B. *Land-Based Wind MARKET Report: 2022 Edition*; Technical Report; Lawrence Berkeley National Lab. (LBNL): Berkeley, CA, USA, 2022.
3. Veers, P.; Dykes, K.; Lantz, E.; Barth, S.; Bottasso, C.L.; Carlson, O.; Clifton, A.; Green, J.; Green, P.; Holttinen, H.; et al. Grand challenges in the science of wind energy. *Science* **2019**, *366*, eaau2027. [[CrossRef](#)] [[PubMed](#)]
4. Hossain, M.L.; Abu-Siada, A.; Muyeen, S.M. Methods for Advanced Wind Turbine Condition Monitoring and Early Diagnosis: A Literature Review. *Energies* **2018**, *11*, 1309. [[CrossRef](#)]
5. Kandil, K.S.A.; Saudi, G.N.; Eltaly, B.A.A.; El-khier, M.M.A. Seismic response of a full-scale wind turbine tower using experimental and numerical modal analysis. *Int. J. Adv. Struct. Eng.* **2016**, *8*, 337–349. [[CrossRef](#)]
6. Ozbek, M.; Rixen, D.J. Operational modal analysis of a 2.5 MW wind turbine using optical measurement techniques and strain gauges. *Wind Energy* **2012**, *16*, 367–381. [[CrossRef](#)]
7. Seidel, M. Auslegung von Hybridtürmen für Windenergieanlagen - Lastermittlung und Nachweis der Ermüdungsfestigkeit am Beispiel einer 3, 6-MW-WEA mit 100 m Rotordurchmesser. *Beton- Und Stahlbetonbau* **2002**, *97*, 564–575. [[CrossRef](#)]
8. Wymore, M.L.; Van Dam, J.E.; Ceylan, H.; Qiao, D. A survey of health monitoring systems for wind turbines. *Renew. Sustain. Energy Rev.* **2015**, *52*, 976–990. [[CrossRef](#)]
9. Bang, H.J.; Kim, H.I.; Lee, K.S. Measurement of strain and bending deflection of a wind turbine tower using arrayed FBG sensors. *Int. J. Precis. Eng. Manuf.* **2012**, *13*, 2121–2126. [[CrossRef](#)]
10. Wondra, B.; Malek, S.; Botz, M.; Glaser, S.D.; Grosse, C.U. Wireless high-resolution acceleration measurements for structural health monitoring of wind turbine towers. *Data-Enabled Discov. Appl.* **2019**, *3*, 4. [[CrossRef](#)]
11. Botz, M.; Oberlaender, S.; Raith, M.; Grosse, C.U. Monitoring of wind turbine structures with concrete-steel hybrid-tower design. In Proceedings of the 8th European Workshop on Structural Health Monitoring (EWSHM), Bilbao, Spain, 5–8 July 2016; pp. 2301–2311.
12. Komarizadehasl, S.; Mobaraki, B.; Ma, H.; Lozano-Galant, J.A.; Turmo, J. Development of a Low-Cost System for the Accurate Measurement of Structural Vibrations. *Sensors* **2021**, *21*, 6191. [[CrossRef](#)]
13. Zieger, T.; Nagel, S.; Lutzmann, P.; Kaufmann, I.; Ritter, J.; Ummerhofer, T.; Knödel, P.; Fischer, P. Simultaneous identification of wind turbine vibrations by using seismic data, elastic modeling and laser Doppler vibrometry. *Wind Energy* **2020**, *23*, 1145–1153. [[CrossRef](#)]
14. Mitka, B.; Klapa, P.; Gniadek, J. Use of terrestrial laser scanning for measurements of wind power stations. *Geomat. Environ. Eng.* **2019**, *13*, 39–49. [[CrossRef](#)]
15. Helming, P.; von Freyberg, A.; Sorg, M.; Fischer, A. Wind Turbine Tower Deformation Measurement Using Terrestrial Laser Scanning on a 3.4 MW Wind Turbine. *Energies* **2021**, *14*, 3255. [[CrossRef](#)]
16. Baqersad, J.; Poozesh, P.; Niezrecki, C.; Avitabile, P. Photogrammetry and optical methods in structural dynamics—A review. *Mech. Syst. Signal Process.* **2017**, *86*, 17–34. [[CrossRef](#)]
17. Ozbek, M.; Meng, F.; Rixen, D.J. Challenges in testing and monitoring the in-operation vibration characteristics of wind turbines. *Mech. Syst. Signal Process.* **2013**, *41*, 649–666. [[CrossRef](#)]
18. Artese, S.; Nico, G. TLS and GB-RAR Measurements of Vibration Frequencies and Oscillation Amplitudes of Tall Structures: An Application to Wind Towers. *Appl. Sci.* **2020**, *10*, 2237. [[CrossRef](#)]
19. Ma, D.; Li, Y.; Liu, Y.; Cai, J.; Zhao, R. Vibration Deformation Monitoring of Offshore Wind Turbines Based on GBIR. *J. Ocean Univ. China* **2021**, *20*, 501–511. [[CrossRef](#)]
20. Baumann-Ouyang, A.; Butt, J.A.; Wieser, A. Bridge deformations during train passage: Monitoring multiple profiles using concurrently operating MIMO-SAR sensors. In Proceedings of the 5th Joint International Symposium on Deformation Monitoring (JISDM), Valencia, Spain, 20–22 June 2022. [[CrossRef](#)]
21. D’Aria, D.; Falcone, P.; Maggi, L.; Cero, A.; Amoroso, G. MIMO Radar-Based System for Structural Health Monitoring and Geophysical Applications. *Int. J. Struct. Constr. Eng.* **2019**, *13*, 258–265.
22. Sun, S.; Petropulu, A.P.; Poor, H.V. MIMO Radar for Advanced Driver-Assistance Systems and Autonomous Driving: Advantages and Challenges. *IEEE Signal Process. Mag.* **2020**, *37*, 98–117. [[CrossRef](#)]
23. Baumann-Ouyang, A.; Butt, J.A.; Salido-Monzú, D.; Wieser, A. MIMO-SAR Interferometric Measurements for Structural Monitoring: Accuracy and Limitations. *Remote Sens.* **2021**, *13*, 4290. [[CrossRef](#)]
24. Pieraccini, M.; Miccinesi, L. An Interferometric MIMO Radar for Bridge Monitoring. *IEEE Geosci. Remote Sens. Lett.* **2019**, *16*, 1383–1387. [[CrossRef](#)]
25. Tian, W.; Li, Y.; Hu, C.; Li, Y.; Wang, J.; Zeng, T. Vibration Measurement Method for Artificial Structure Based on MIMO Imaging Radar. *IEEE Trans. Aerosp. Electron. Syst.* **2019**, *56*, 748–760. [[CrossRef](#)]
26. Miccinesi, L.; Consumi, T.; Beni, A.; Pieraccini, M. W-band MIMO GB-SAR for Bridge Testing/Monitoring. *Electronics* **2021**, *10*, 2261. [[CrossRef](#)]
27. Hu, C.; Deng, Y.; Tian, W.; Wang, J.; Zeng, T. Novel MIMO-SAR system applied for high-speed and high-accuracy deformation measurement. *J. Eng.* **2019**, *2019*, 6598–6602. [[CrossRef](#)]

28. Pham, T.H.; Kim, K.H.; Hong, I.P. A Study on Millimeter Wave SAR Imaging for Non-Destructive Testing of Rebar in Reinforced Concrete. *Sensors* **2022**, *22*, 8030. [[CrossRef](#)]
29. Broussolle, J.; Kyovtorov, V.; Basso, M.; Ferraro Di Silvi E Castiglione, G.; Figueiredo Morgado, J.; Giuliani, R.; Oliveri, F.; Sammartino, P.F.; Tarchi, D. MELISSA, a new class of ground based InSAR system. An example of application in support to the Costa Concordia emergency. *ISPRS J. Photogramm. Remote Sens.* **2014**, *91*, 50–58. [[CrossRef](#)]
30. Hosseiny, B.; Amini, J.; Safavi-Naeini, S. Simulation and Evaluation of an mm-Wave MIMO Ground-Based SAR Imaging System for Displacement Monitoring. In Proceedings of the 2021 IEEE International Geoscience and Remote Sensing Symposium IGARSS, Brussels, Belgium, 11–16 July 2021; pp. 8213–8216. [[CrossRef](#)]
31. Hosseiny, B.; Amini, J.; Aghababaei, H. Structural Displacement Monitoring Using Ground-based Synthetic Aperture Radar. *Int. J. Appl. Earth Obs. Geoinf.* **2022**, *116*, 103144. [[CrossRef](#)]
32. Texas Instruments Inc. *Imaging Radar Using Cascaded mmWave Sensor Reference Design*; Texas Instruments Inc.: Dallas, TX, USA, 2019.
33. Calandawind. Windenergieanlage. Available online: <https://www.calandawind.ch/windenergieanlage/> (accessed on 6 November 2022).
34. Vestas Wind Systems A/S. Vestas V112 3.0 MW ONSHORE. 2011. Available online: https://www.wind-still.ch/files/windstill/files/pdf/Vestas_V112_web_DE.pdf (accessed on 6 November 2022).
35. Texas Instruments Inc. *mmWave Studio Cascade—User Guide*; Texas Instruments Inc.: Dallas, TX, USA, 2019.
36. Balestrieri, E.; Vito, L.D.; Picariello, F.; Rapuano, S.; Tudosa, I. A review of accurate phase measurement methods and instruments for sinewave signals. *ACTA IMEKO* **2020**, *9*, 52. [[CrossRef](#)]
37. Yu, H.; Lan, Y.; Yuan, Z.; Xu, J.; Lee, H. Phase Unwrapping in InSAR: A Review. *IEEE Geosci. Remote Sens. Mag.* **2019**, *7*, 40–58. [[CrossRef](#)]
38. Baumann-Ouyang, A.; Butt, J.A.; Wieser, A. Estimating 3D displacement vectors from line-of-sight observations with application to MIMO-SAR. *J. Appl. Geod.* **2023**, *accepted*.
39. Gauss, C.F. *Theoria Motus Corporum Coelestium in Sectionibus Conicis Solem Ambientium*; Perthes, F., Besser, I.H., Eds.; FA Perthes: Hamburg, Germany, 1809; pp. 1–227. [[CrossRef](#)]
40. Legendre, A.M. *Nouvelles Méthodes pour la Détermination des Orbites des Comètes: Avec un Supplément Contenant Divers Perfectionnements de ces Méthodes et leur Application aux deux Comètes de 1805*; Courcier: Paris, France, 1806.
41. Ferretti, A.; Prati, C.M.; Rocca, F. Permanent scatterers in SAR interferometry. *IEEE Trans. Geosci. Remote Sens.* **2001**, *39*, 8–20. [[CrossRef](#)]
42. Touzi, R.; Lopes, A.; Bruniquel, J.; Vachon, P.W. Coherence estimation for SAR imagery. *IEEE Trans. Geosci. Remote Sens.* **1999**, *37*, 135–149. [[CrossRef](#)]
43. Richards, M.A.; Scheer, J.; Holm, W.A.; Melvin, W.L. *Principles of Modern Radar*; Citeseer: New York, NY, USA, 2010; Volume 1.
44. Kingsley, S.; Quegan, S. *Understanding Radar Systems*; SciTech Publishing: Raleigh, NC, USA, 1999; Volume 2, ISBN 1-891-12105-7.
45. *IEEE Standard 952*; IEEE Standard Specification Format Guide and Test Procedure for Single-Axis Interferometric Fiber Optic Gyros. Institute of Electrical and Electronics Engineers: New York, NY, USA, 1997.

Disclaimer/Publisher’s Note: The statements, opinions and data contained in all publications are solely those of the individual author(s) and contributor(s) and not of MDPI and/or the editor(s). MDPI and/or the editor(s) disclaim responsibility for any injury to people or property resulting from any ideas, methods, instructions or products referred to in the content.